Deconvolution Methods for Mitigation of Transverse Blurring in Optical Coherence Tomography

Tyler S. Ralston, *Associate Member, IEEE*, Daniel L. Marks, Farzad Kamalabadi, *Member, IEEE*, and Stephen A. Boppart, *Member, IEEE*

***Abstract*—Imaging resolution in optical coherence tomography (OCT) is a key determinant for acquiring clinically useful optical biopsies of tissues. In contrast to light or confocal microscopy, the axial and transverse resolutions in OCT are independent and each can be analyzed individually. A method for mitigating transverse blurring and the apparent loss of transverse resolution in OCT by means of Gaussian beam deconvolution is presented. Such a method provides better representation of a specimen by using known physical parameters of a lens. To implement this method, deconvolution algorithms based on a focal-dependent kernel are investigated. First, the direct inverse problem is investigated using two types of regularization, truncated singular value decomposition, and Tikhonov. Second, an iterative expectation maximization algorithm, the Richardson–Lucy algorithm, with a beam-width-dependent iteration scheme is developed. A dynamically iterative Richardson–Lucy algorithm can reduce transverse blurring by providing an improvement in the transverse point-spread-function for sparse scattering samples in regions up to two times larger than the confocal region of the lens. These deblurring improvements inside and outside of the confocal region, which are validated experimentally, are possible without introducing new optical imaging hardware or acquiring multiple images of the same specimen. Implementation of this method in sparse scattering specimens, such as engineered tissues, has the potential to improve cellular detection and categorization.**

***Index Terms*—Deconvolution, focusing, Gaussian beam, Richardson–Lucy, transverse resolution.**

I. Introduction

THE ABILITY to visualize cellular features in tissue is both clinically important for disease diagnosis and scientifically important for understanding fundamental biological processes. A central component to the pathological examination of cellular features is the visualization of the nucleus, including its shape, contours, inclusions, optical staining and light-scattering properties, and its size, especially in relation to the cytoplasm within the cell [1]. Various stages of dysplasia and neoplasia are based primarily on the nuclear-to-cytoplasmic (N/C) ratio, and determining this ratio for regions in tissue can have a significant life-determining impact on the diagnosis, the prognosis, and the treatment regimen. The gold-standard for the microscopic investigation of pathology is the use of stained histological sections from resected tissues, observed most commonly with light microscopy. The use of selective stains on micron-thin tissue sections enables pathologists to highlight and visualize nuclear features with ease.

In many medical and surgical scenarios, it may be more advantageous to visualize cellular features *in vivo*, without the need to invasively sample, process, section, and stain tissue specimens to make a diagnosis. In addition, the increasing interest in tissue engineering has prompted the need to more fully visualize and understand the complex process of tissue development under controlled conditions and in three dimensions, including the need to understand how cells function, proliferate, and organize into biocompatible tissues [2]. Advanced optical imaging techniques have been developed to improve our ability to visualize cellular features, including confocal, multiphoton microscopy, and optical coherence tomography (OCT).

OCT is an emerging, real-time, near-infrared imaging and microscopy technique capable of micrometer-scale resolutions in biological specimens [3]–[5]. OCT is based on the detection of backscattered light from tissue and is analogous to ultrasound imaging except near-infrared light is detected rather than sound. OCT can perform *in vivo* imaging deep within highly scattering tissues due to its ability to coherently reject multiply-scattered photons, and can image tissue without the addition of exogenous contrast agents. While OCT can generate cellular-level resolution images, the technique does not currently have the advantage of using selective stains or contrast agents to label and improve visualization of cell nuclei as in histopathology. Visualization of cell nuclei using OCT is based on the optical scattering properties of the cell and its local environment [6]. Therefore, techniques that can be developed to improve the visualization of cells and nuclei will not only advance the use of OCT for medical and surgical diagnostic applications [7], but also enable OCT to visualize complex cellular processes deep within three-dimensional (3-D) engineered tissue constructs [8].

The ability to visualize cells and cellular features with OCT depends primarily on achieving high imaging resolution and preserving narrow point-spread-functions in the axial and transverse directions. Axial resolution is dependent on the optical

Manuscript received December 19, 2004; revised May 20, 2005. This work was supported in part by the National Institutes of Health (1 R01 EB00108-1, S.A.B.) and in part by the Beckman Institute for Advanced Science and Technology (T.S.R.). The animals used in this research were handled and cared for under the approved protocols of the Institutional Animal Care and Use Committee at the University of Illinois Urbana-Champaign. The associate editor coordinating the review of this manuscript and approving it for publication was Dr. Gaudenz Danuser.

T. S. Ralston and D. L. Marks are with the Beckman Institute for Advanced Science and Technology and the Department of Electrical and Computer Engineering, University of Illinois at Urbana-Champaign, Urbana, IL 61801 USA (e-mail: tralston@uiuc.edu; dmarks@uiuc.edu).

F. Kamalabadi is with the Department of Electrical and Computer Engineering and the Coordinated Science Laboratory, University of Illinois at Urbana-Champaign, Urbana, IL 61801 USA (e-mail: farzadk@uiuc.edu).

S. A. Boppart is with the Beckman Institute for Advanced Science and Technology, Department of Electrical and Computer Engineering, Department of Bioengineering, and College of Medicine, University of Illinois at Urbana-Champaign, Urbana, IL 61801 USA (e-mail: boppart@uiuc.edu).

Digital Object Identifier 10.1109/TIP.2005.852469

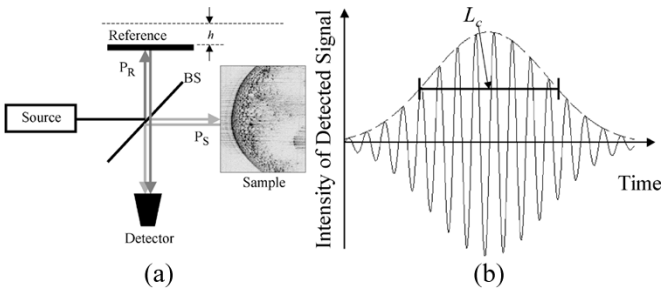

Fig. 1. (a) Michelson interferometer setup for use in OCT. P_R is the reference path, P_S is the sample path, BS is the beam splitter, and h is the distance traveled by the reference mirror. (b) Interferogram of an impulse response for an OCT system with a low coherence source having a Gaussian spectrum and coherence length L_c.

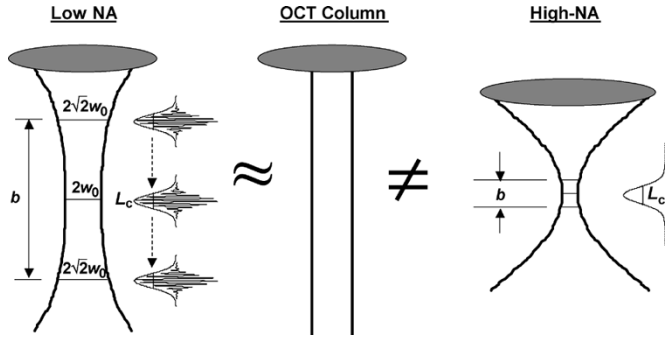

Fig. 2. Geometry of a Gaussian beam for low and high NA lenses. These geometries are contrasted with the assumption of a collimated axial OCT scan. b is the confocal parameter, w_o is the beam radius at the focus, and L_c is the coherence length of the source.

coherence in an OCT system and inversely proportional to the spectral bandwidth of the optical source. Conceptually, optical coherence is related to the wave field interactions. At optical frequencies, first-order field quantities fluctuate too rapidly to be detected directly. A direct detection method can only result in collecting data for mean power quantities over time periods far greater than the length of the period for a field. Therefore, by assuming ergodicity in the mean, mean square, or correlation function of the fields, the corresponding time-averages converge to the named ensemble averages. To facilitate these measurements, typically a Michelson interferometer is employed in an OCT system [Fig. 1(a)]. As the mirror in the reference arm moves, the light coming into the detector varies between states of constructive interference and destructive interference. A plot of the intensity versus difference in reference and sample path lengths is called an *interferogram*; it is the cross-correlation signal. Fig. 1(b) is a portion of an interferogram displaying the point-spread function (PSF) for a single perfect reflector, such as a mirror. The interferogram is a real signal; thus, it has positive and negative frequencies. The interferogram can be used to generate a complex analytic signal that contains only positive frequencies. This is useful in OCT for generating phase and magnitude information which are used to generate Doppler OCT and structural OCT images, respectively [9]–[11]. The complex analytic signal is most relevant when deciding the feasibility of each algorithm presented in the following sections. Namely, some algorithms have positivity constraints [12], [13], which do not apply to OCT refractive index reconstruction, but still may be useful when imaging point-like scatterers.

The coherence length L_c is a measure of the full-width at half-maximum (FWHM) of the interferogram envelope, which is inversely proportional to the spectral bandwidth of the optical source. Thus, the coherence length directly determines the axial resolution in OCT images and for a Gaussian spectrum, the free-space axial resolution is given by

$$L_c = \frac{2(\ln 2)\lambda_o^2}{\pi \Delta\lambda} \tag{1}$$

where λ_o is the central wavelength and $\Delta\lambda$ is the FWHM of the power spectrum. The equation implies that either a shorter wavelength or a wider bandwidth of the power spectrum $\Delta\lambda$ is needed to achieve a higher axial resolution.

OCT images are typically formed by assembling adjacent axial scans to generate a two-dimensional, cross-sectional image [4], [5]. Ideally, the beam is perfectly collimated at every point in the sample. However, in the Gaussian optics model, the geometry of the beam profile after passing through a lens exhibits an hourglass shape as illustrated in Fig. 2. This profile assumes a Gaussian beam with a direction of propagation incident normal to the lens. The limitation of the Gaussian beam model compared to the physical reality is that usually when light enters the sample, the index of refraction varies, thus distorting the profile. Therefore, the transverse resolution is not constant, but has a dependence on the depth and the focal region of the lens. Lenses with a higher numerical aperture (NA) are able to focus a beam to a smaller spot size but produce a more pronounced hourglass shape. Hence, high NA lenses are typically used for optical sectioning in planes parallel (*en face*) to the surface of the specimen such as in confocal or multiphoton microscopy [14]. Lenses with a lower NA are typically used for OCT, where a relatively uniform transverse resolution over the entire axial (depth) scan is preferred. Typically in OCT, the confocal parameter (distance about the focus where the beam width is relatively uniform) is chosen to closely match the depth of imaging penetration in a particular tissue type.

The transverse resolution R_T is characterized by the beam profile incident on the sample and the confocal parameter b. The transverse resolution is determined by the diameter of the spot size $2w_o$ or the width of the incident beam on the sample where the edges are determined by a decrease in intensity by a factor of $1/e^2$ and is approximated by

$$R_T \approx 2w_o \approx 2.44\frac{f\lambda_o}{D} \tag{2}$$

where f is the focal length of the lens, D is the beam diameter incident on the objective lens, and λ_o is the central wavelength. The confocal parameter can be defined as

$$b = \frac{\pi R_T^2}{2\lambda_o}. \tag{3}$$

Equation (3) indicates that the size of the confocal region decreases as the square of the transverse resolution increases. Transverse resolution is significantly reduced and features are blurred outside of the confocal region. In OCT, the focusing

Gaussian beam profile remains fixed, while varying the reference arm pathlength scans the depth at which backscattered signal is detected. In OCT images, if a high NA objective is used and the depth scan length exceeds the dimension of the confocal region, then the widening of the transverse PSF will be evident in the image and features located outside of the confocal region will appear blurred. Our motivation for this research is to digitally reduce the transverse blurring outside of the confocal region by using deconvolution techniques. The solution will be to first determine how OCT measurements depend on the object when blurred with a Gaussian beam, and then find a suitable estimate of the original object.

A diversity of deconvolution algorithms has been developed for estimating a genuine signal based on idealizations of physical properties. For instance, the astronomy community has developed several algorithms, which have proven to be important for extracting relevant information [15]. Furthermore, optical microscopy has benefited from use of these restoration techniques, which solve problems such as out-of-focus flare in fluorescence imaging [16]. Several deconvolution algorithms have been implemented in OCT to correct for axial blurring [17]–[19]. The deconvolution employed in these papers is based on the blurring induced by the incident electric field convolved with the impulse response of an object. The primary deconvolution techniques that have been used are the constrained iterative restoration algorithm and the minimum-norm least-squares-error linear solution. These algorithms are designed for a single axial scan only and do not incorporate information as defined by the Gaussian optics model. Experimental setups have utilized additional optical hardware such as adaptive optics or axicon lenses to increase the transverse resolution over large depths in the specimen [20], [21]. Dynamic focusing techniques have been implemented for OCT and optical coherence microscopy to generate images with high transverse resolutions over relatively large depths, which can be useful for *en face* imaging [4], [22]. Although these methods are feasible, each requires specific hardware modifications that can be expensive or difficult to control in the OCT system setup. One algorithm for generating OCT images with high transverse resolution over large apparent depth scans involves composite (C-mode) imaging [23], and is analogous to one used in ultrasound imaging. This algorithm involves the acquisition of multiple OCT images, with the beam focus placed at incrementally increasing depths within the specimen. From each image, data located within the short confocal region is segmented out and subsequently assembled to produce a single composite image. A significant advantage of the transverse deconvolution algorithm presented here is the reduction of the transverse blurring and the apparent improvement in transverse resolution inside and outside of the confocal region without the addition of new optical hardware or the need to acquire multiple images of the same specimen.

The main objective of this paper is to investigate a set of algorithms for reducing the transverse blurring within an OCT image by deconvolving the Gaussian beam blurring caused by a lens. The next section demonstrates a general approach to modeling the physical parameters that characterize the lens. Then, a number of solutions to remove the effect of the Gaussian beam blur are discussed. Furthermore, simulations for each of these solutions are used to assess algorithm performance. Finally, the algorithms are applied to experimentally acquired OCT images to further characterize the Gaussian beam problem.

A more uniform PSF throughout an image can impact the way an object is categorized. For example, a biological specimen with pre-cancerous cellular changes may go unnoticed if it lies in an imaging region where the blurring occurs [24], [25], and a varying PSF could result in a misdiagnosis [26]. Finally, there is the potential for reducing data acquisition time since a higher percentage of the OCT image may be more clinically useful.

II. Physical Model

To analyze the transverse PSF in OCT, it is necessary to create an accurate mathematical model of the transverse beam dynamics in the OCT system. Specifically, the Gaussian beam profile of the lens characterizes the depth-dependent transverse resolution. A Gaussian beam $G(\vec{r})$ with a 3-D vector position $\vec{r}$ can be represented by the following equation:

$$G(\vec{r}) = A_0 \frac{W_0}{W(z)} \exp\left(-\frac{\rho^2}{W^2(z)}\right) \times \exp\left(-jk(\omega)z - jk(\omega)\frac{\rho^2}{2R(z)} + j\zeta(z)\right) \quad (4)$$

where the Guoy phase shift is

$$\zeta(z) = \tan^{-1}\left(\frac{z}{z_0}\right) \quad (5)$$

the radius of curvature of the wavefront is given by

$$R(z) = z\left(1 + \left(\frac{z_0}{z}\right)^2\right) \quad (6)$$

the depth dependent beam waist size is given by

$$W(z) = W_0\left[1 + \left(\frac{z}{z_0}\right)^2\right]^{\frac{1}{2}} \quad (7)$$

the radius in Cartesian coordinates is given by

$$\rho = \sqrt{x^2 + y^2} \quad (8)$$

and the optical source wavenumber (neglecting dispersion) is given by

$$k(\omega) = k_0 + \frac{\omega - \omega_0}{v_g} \quad (9)$$

where v_g is the group velocity (envelope speed), A_0 is a constant amplitude, k_0 is the center wavenumber, ω_0 is the center frequency, ω is the frequency of the light, W_0 is the waist radius, x and y are the transverse coordinates, and z is the axial coordinate where $z = z_0$ at the boundary of the confocal region [27]. The phase-front emitted from a scattering object in the Gaussian beam has a curvature dependent on the phase term $-jk(\rho^2/2R(z))$. The phase-fronts are approximately planar at

the beam waist, but become increasingly parabolic at distances away from the waist (outside of the confocal region). At distances even farther from the beam waist, the Gaussian phase-front has approximately spherical constant-time surfaces. In this work, all of the phase-fronts are approximated as planar since the areas near the confocal region are of primary interest. Fig. 3 shows the curved phase-fronts in gray and the planar phase-fronts as dashed lines. Rewriting the Gaussian beam equation for planar phase-fronts gives

$$G(x,y,z) = \frac{W_0}{W(z)} \exp\left(-\frac{x^2+y^2}{W^2(z)}\right) \times \exp\left(-j\left(k_0 + \frac{\omega-\omega_0}{v_g}\right)z\right). \quad (10)$$

The first Born approximation is usually sufficient to accurately reconstruct an OCT image. Fig. 3 also diagrams the first Born approximation as applied to the Gaussian beam deconvolution problem. The Green's function is given by $\Gamma(\vec{r})$ and represents the reflection due to a change in index in the object being imaged, $\Delta\eta(\vec{r})$. The Gaussian beam profile is given by $G(\vec{r}-\vec{r}_s)$, where $\vec{r}_s$ is the distance from the center of the lens. Thus, a first Born (single scattering) approximation of the electric field scattered by the object is given by

$$R(\vec{r}) = \Gamma(\vec{r}) * (\Delta\eta(\vec{r}) \cdot G(\vec{r}-\vec{r}_s)) \quad (11)$$

where $*$ denotes 3-D spatial convolution and

$$\Gamma(\vec{r}) = \frac{1}{4\pi}\frac{\exp\left(j\frac{2\pi}{\lambda}|\vec{r}|\right)}{|\vec{r}|}. \quad (12)$$

A single axial scan of OCT data can be written as the projection of reflected light returning into the lens from the Gaussian beam. $\tilde{S}(r_s,\omega)$ is the amplitude of the collected electric field scaled relative to the incident field that has been scattered by the object

$$\tilde{S}(r_s,\omega) = \int G(\vec{r}-\vec{r}_s)\left[\Gamma(\vec{r}) * (\Delta\eta(\vec{r})G(\vec{r}-\vec{r}_s))\right] d\vec{r}. \quad (13)$$

Notice that $G(\vec{r})$ and $\Gamma(\vec{r})$ are also functions of ω. When the spherical waves from the Gaussian beam are scattered off of the object, they are matched to the mode re-entering the fiber. Thus, $\Gamma(\vec{r})$ is approximated by a delta function on the k sphere. The field collected by the fiber is approximated in the paraxial zone by

$$\tilde{S}(\vec{r}_s,\omega) = \int \Delta\eta(\vec{r})\left[G(\vec{r}-\vec{r}_s)\right]^2 dr. \quad (14)$$

Note that the square operation in (14) is on the complex Gaussian beam profile, and not its squared magnitude. Next, by integrating over the frequencies present in the bandwidth of the laser, where $I(\omega)$ is the power spectral density, we can generate a formula for the axial scan data as a function of time and space

$$\tilde{S}(x_s,y_s,t) = \int \tilde{S}(x_s,y_s,\omega)I(\omega)e^{-j\omega t}\, d\omega. \quad (15)$$

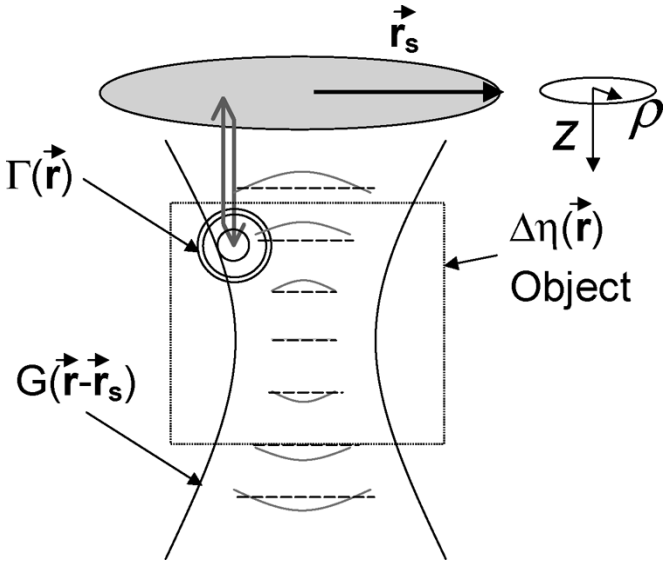

Fig. 3. Gaussian beam wavefronts (solid gray) from nonlinear exponential quantities and an approximation (dashed) with the quantities removed, $\vec{r}_s$ is the vector from the center of the lens to a scatterer, $G(\vec{r})$ is the Gaussian envelope, $\Gamma(\vec{r})$ is the Green's function, and $\Delta\eta(\vec{r})$ is the index of refraction change in the imaged medium. Vertical arrows represent the incident and reflected light path for the first Born approximation (single backscatter).

Equation (15) can be rewritten using (14) and (10) to get

$$\tilde{S}(x_s,y_s,t) = \int \left(\frac{W_0}{W(z)}\right)^2 \exp\left(-2j\left(k_0+\frac{\omega_0}{v_g}\right)z\right) I\left(t-\frac{2z}{v_g}\right) \times \left[\int\int \Delta\eta(\vec{r}) \times \exp\left(-2\frac{((x-x_s)^2+(y-y_s)^2)}{W^2(z)}\right)dxdy\right]dz \quad (16)$$

where $I(t-(2z/v_g))$ produces coherence gating, the quantity in square brackets represents a separable Gaussian convolution kernel having a depth-dependent standard deviation $W(z)$, and the remaining terms represent a depth-dependent magnitude and phase. The coherence gating, the magnitude, and the phase in (16) are only depth dependent and, thus, not dependent on the transverse coordinates. Therefore, the convolution integral of electric fields can be treated as a convolution integral of intensities, which can be considered separately [17]. The separable Gaussian kernel allows us to estimate a y-blurred version of the object for an axial scan, $\tilde{S}(x_s,t)$. Namely, the bracketed quantity in (16), which contains the convolution integral of the transverse coordinates, can be rewritten as

$$\int\left[\int \Delta\eta(x_s,y_s,z)\exp\left(-2\frac{(y-y_s)^2}{W^2(z)}\right)dy\right] \times \exp\left(-2\frac{(x-x_s)^2}{W^2(z)}\right)dx \quad (17)$$

where the new bracketed term is a y-blurred version of the object and can be denoted by $\Delta\eta'(x_s,z)$. Thus, by applying a deconvolution algorithm to each of the approximated Gaussian kernels

in the x direction, the object can be reconstructed with blurring in only the y direction.

Equation (17) applies to any index of refraction distribution, $\Delta\eta'(x_s, z)$. To this point, the forward problem has been described where the fringe data retrieved is complex analytic. In some cases, for use with a positivity-constrained algorithm or with an intermediary demodulation circuit, signal analysis of the magnitude data is desired. Also, for objects consisting of sparse point-like scatterers, such as would be the case for cells distributed in a 3-D engineered tissue matrix, the points will be sufficiently angularly or axially separated so that the point responses will not overlap in the interferogram. Thus, the magnitude of the interferogram can then be approximated by summing the magnitudes of the interferograms of the constituent points separately, rather than the full complex signals. In this case, we approximate (17) as a convolution of magnitudes

$$\int \left| \int \Delta\eta(x_s, y_s, z) \exp\left(-2\frac{(y-y_s)^2}{W^2(z)}\right) dy \right| \times \left| \exp\left(-2\frac{(x-x_s)^2}{W^2(z)}\right) \right| dx. \quad (18)$$

Similarly, deconvolving each of the magnitude Gaussian kernels in the x direction, the object can be reconstructed with blurring in only the y direction. The y-blurred image represents the cross-sectional OCT image, which is scanned along the x and z directions. Since the Gaussian kernel is separable, the deconvolution could also be computed for the x-blurred image, along the y and z directions. This physical model of the Gaussian beam can now be used in context with our proposed algorithms.

III. Methodology

The physical model is a linear system that takes the general form $\tilde{S}(x_s, y_s, t) = A_z \Delta\eta(x_s, y_s, z)$, where A_z is a depth-dependent linear operator. For simplicity, the forward problem will be defined for each depth as $y = Ax + n$, where y is a row of the OCT signal $\tilde{S}(x_s, y_s, t)$, x is the row-wise refractive index of the object $\Delta\eta(x_s, y_s, z)$, A is the depth z, dependent Gaussian beam blurring operator, and n is noise generated by electronic or shot noise contributions. Note, A is the convolution matrix associated with each depth-dependent K-tap Gaussian filter, where $h_n = \exp(-2n^2/W^2(z))$ from (17), and the singular value decomposition (SVD) is given by

$$A \triangleq \begin{bmatrix} h_0 & 0 & \cdots & 0 \\ h_1 & h_0 & \ddots & \vdots \\ \vdots & h_1 & \ddots & 0 \\ h_{K-1} & \vdots & \vdots & h_0 \\ 0 & h_{K-1} & \ddots & h_1 \\ \vdots & \ddots & \ddots & \vdots \\ 0 & \cdots & 0 & h_{K-1} \end{bmatrix} = U\Sigma V^H = \sum_{i=1}^{n} u_i \sigma_i v_i^H \quad (19)$$

where U and V are a set of orthonormal vectors and u_i and v_i column vectors, respectively, for the diagonal matrix Σ of singular values σ_i.

For the underdetermined case, an optimal criterion considered is the minimum norm solution, which will minimize the variance

$$x_{MN} = A^H (AA^H)^{-1} y = \sum_{i=1}^{n} \frac{u_i^H y}{\sigma_i} v_i. \quad (20)$$

This solution is precisely the pseudoinverse [28].

Since this design models noise, there will be a need for a regularized solution; otherwise, the solution will be overly sensitive to changes in the OCT signal due to noise. Next, the truncated SVD (TSVD) is used to provide a regularized solution

$$x_{\mathrm{TSVD}} = \sum_{i=1}^{k} \frac{u_i^H y}{\sigma_i} v_i \quad (21)$$

where k is determined by a regularization parameter, α, which is a corresponding threshold such that all $\sigma_i > \alpha$ are retained [29]. This method is chosen because it reduces the emphasis on smaller singular values in the minimum norm solution, which are more correlated to the noise. Tikhonov regularization is also employed

$$x_{Tikh} = \left(A^H A + \lambda L^H L\right)^{-1} A^H y \quad (22)$$

where λ is a regularization parameter, which can be estimated to be half the noise variance for a reasonable solution when L is the identity matrix [30]. There exist methods for a robust data dependent L, but prior numerical experiments justify our choice of L as being the identity matrix [31]. Tikhonov regularization offers a method for compromising between the size of the residual norm and the side constraint λ. Thus

$$x_{Tikh} = \sum_{i=1}^{n} \frac{\sigma_i^2}{\sigma_i^2 + \lambda^2} \frac{u_i^H y_i}{\sigma_i} v_i. \quad (23)$$

An iterative deconvolution scheme, known as Richardson–Lucy, converges to the maximum likelihood solution for Poisson statistical data, which is appropriate in some cases for modeling optical data that has shot noise, a result of counting statistics [32]. Each pixel in the reconstructed image is updated on every iteration. The algorithm is implemented in the following manner:

$$\hat{x}_{n+1,i} = \hat{x}_{n,i} \sum_j \frac{h_{j-i+1} y_j}{\sum_k h_{j-k+1} \hat{x}_{n,k}} \quad (24)$$

where h_n is the PSF, in this case, the Gaussian blurring kernel [12], [13]. This method forces the restored image to be positive for each iteration. Thus, the use of complex analytic data as retrieved from OCT may not be fully utilized. However, since a magnitude image is a subsampled version of the subresolution

complex analytic signal, the complex information may be neglected in the case of transverse blurring for the reconstructed image as shown in (18).

The Richardson–Lucy algorithm has been shown to monotonically reduce the Csiszár's I-divergence for successive iterations between the measured blurred image and a blurred version of the estimated image [33]. Unfortunately, once the I-divergence between iterations is minimized, the effect of additional iterations only serves to introduce error. For this reason, we would like to have an algorithm that adapts to the amount of defocus in the image. Thus, an iteration number having a dependence directly related to the standard deviation of the Gaussian blurring kernel is appropriate. The dynamic iteration method was developed empirically in simulations and applied accordingly for the real data.

Performing convolution as a zero-padded cyclic convolution in the Fourier domain decreases the computational expense of these algorithms. The Richardson–Lucy algorithm often requires multiple iterations, thus increasing the computational expense compared to the regularization algorithms.

IV. Simulations

The simulations of the OCT system follow a method developed by Marks, *et al.* [18]. In this OCT model, filtering the interferogram with an appropriate laser spectrum simulates the axial resolution.

To create simulation fringes similar to OCT for a set of point (delta) scatterers, (reflections from subresolution-sized particles), four parameters must be taken into account.

1) The point scatterers have random phase (to model random positions of particles situated within a coherence volume).
2) The system has bandwidth support limited by the laser spectrum (bandwidth of 100 nm, centered at 820 nm).
3) The lens creates a Gaussian beam depth-dependent transverse blur (focal length of $f = 5$ mm, spot size of $2w_o = 5\ \mu$m, confocal parameter of $b = 48\ \mu$m, and diameter of beam on the lens of $D = 2$ mm).
4) The system has Gaussian white noise (SNR $= 35$ dB).

After creating point scatterers, the first parameter above is easily simulated by multiplying each of the scatterers by a random phase value. Next, the band-limited support on the signal defines the axial resolution of the system. Therefore, the column data is band limited by taking the fast Fourier transform (FFT), multiplying by an appropriate filter ($\Delta\lambda = 100$ nm) with cut offs at $1/\lambda_{\max}$ and $1/\lambda_{\min}$, and then taking the inverse FFT (IFFT). The effects of these two parameters can be seen in Fig. 4(a) and represent our deblurred and denoised image where delta scatterers are oversampled in the axial direction.

Next, to simulate the Gaussian beam blurring, which would be caused by a lens as described in (16), a matrix is created where each row is a depth-dependent PSF. Thus, each row of the image is convolved with the corresponding Gaussian kernel whose standard deviation is given in (7). Finally, to generate a noisy version y_n of the simulation image y

$$y_n = y + w; \quad w \sim N(0, \sigma^2 I) \tag{25}$$

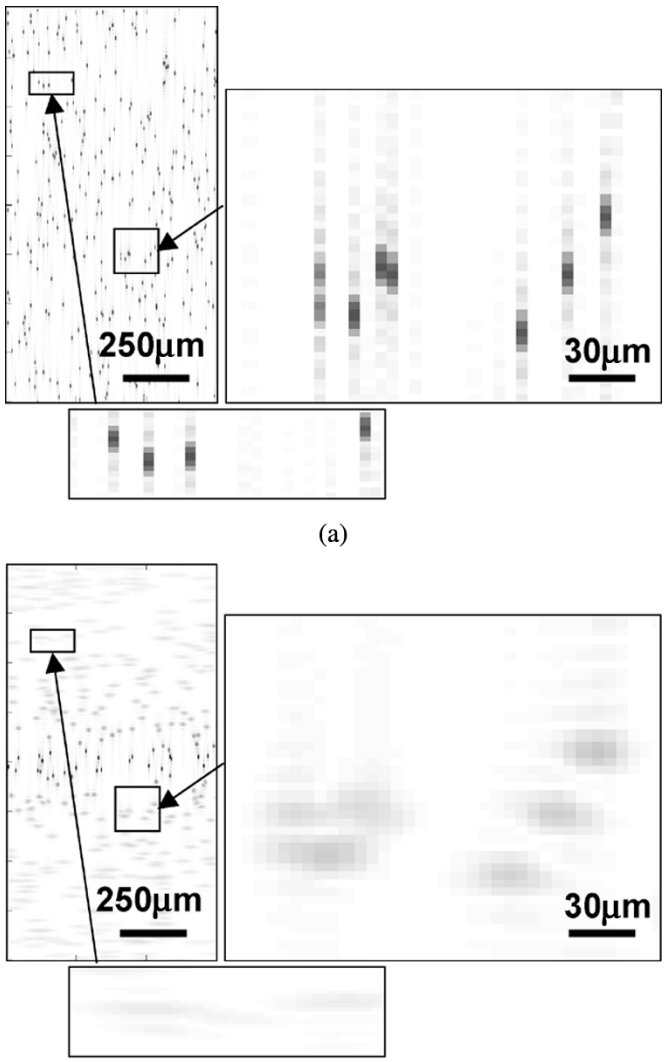

Fig. 4. Simulated OCT image of oversampled point scatterers. (a) Before (left) a Gaussian beam blur and (right, bottom) zoom on scatterers, when parameters 1 and 2 are satisfied. (b) After (left) a Gaussian beam blur and (right, bottom) zoom on scatterers, with SNR $= 35$ dB, and when parameters 3 and 4 are satisfied.

where w is a vector of independent identically distributed noise samples. The signal-to-noise ratio (SNR) is determined by the variance of the image, σ_y^2, over the variance of the noise σ_n^2

$$\text{SNR(dB)} = 10 \cdot \log_{10}\left(\frac{\sigma_y^2}{\sigma_n^2}\right). \tag{26}$$

The standard deviation of the noise, σ_n, was determined for a SNR value of 35 dB, which is less than the typical dynamic range for data contained within an OCT image. The methodology for this testing is to characterize the resilience of the algorithm. Testing algorithms with a low SNR serves to evaluate the algorithm performance and determine useful regularization parameters. The resulting image after addition of Gaussian blurring and white noise is seen in Fig. 4(b). All simulated figures have the same scatterers at the same positions for direct comparison.

The pseudoinverse with TSVD regularization was used to generate the minimum norm solution using both the magnitude

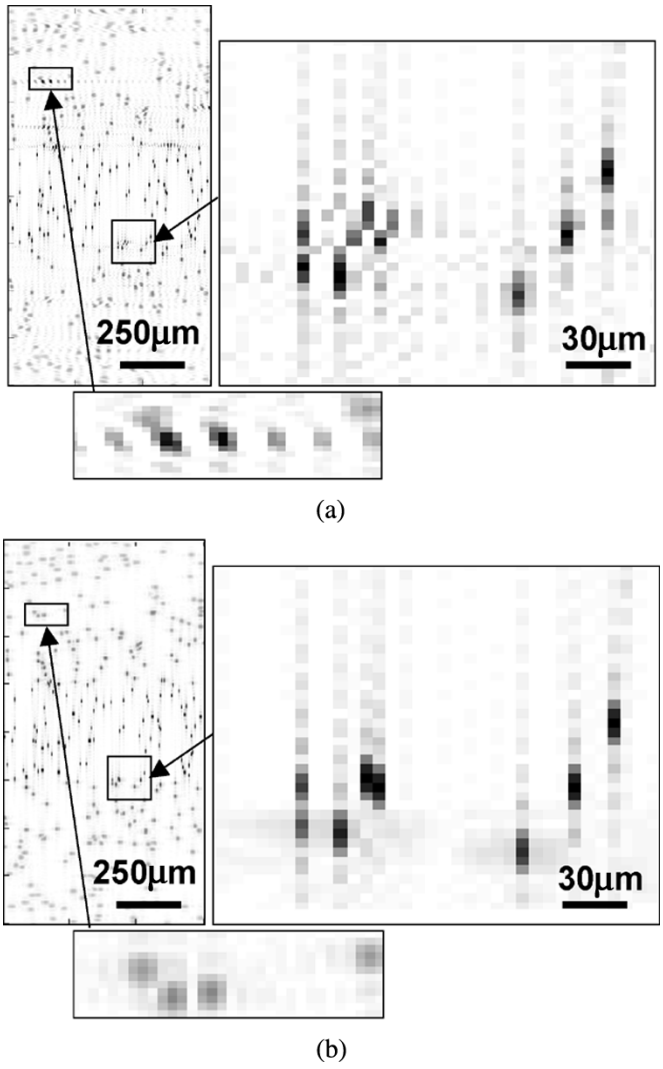

Fig. 5. TSVD, $\alpha = 0.01$, SNR $= 35$ dB, using (a) magnitude signal (ringing artifacts) and (b) complex analytic signal (minimal ringing).

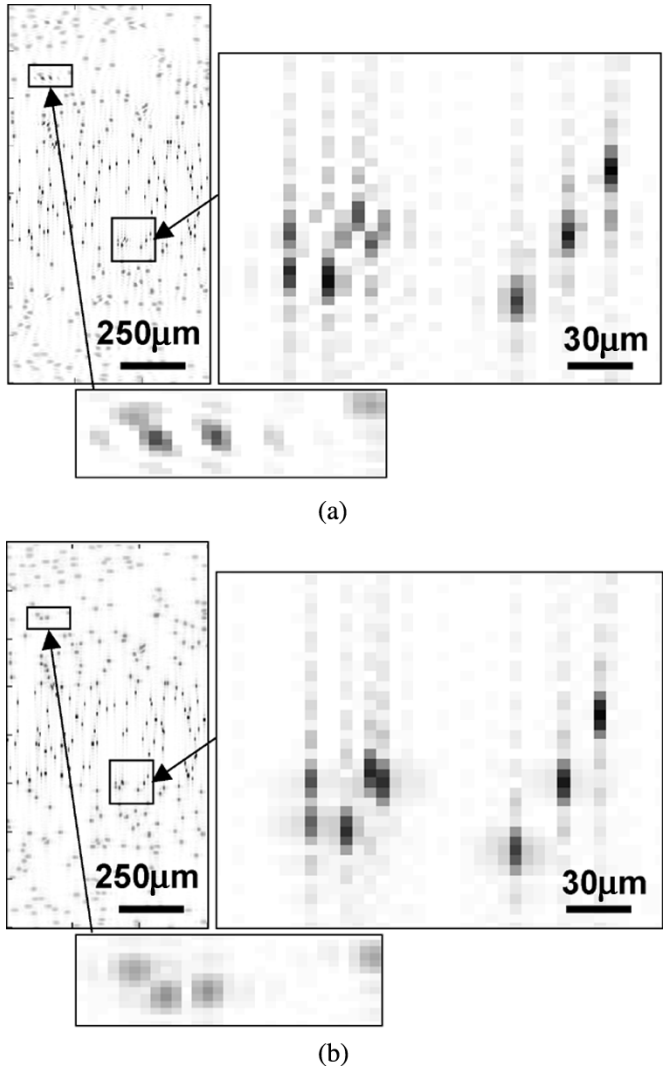

Fig. 6. Tikhonov regularization, $\lambda = 0.02$, SNR $= 35$ dB, using (a) magnitude signal (some ringing artifacts) and (b) complex analytic signal (minimal ringing).

and complex analytic fringe data. Several values for the regularization parameter were explored, but $\alpha = 0.01$ optimally balanced the noise with the reconstruction (verified with the Picard condition) [34]. Fig. 5(a) shows the reconstruction based on only the magnitude data. Reconstruction artifacts such as ringing are quite apparent in this image, whereas the reconstruction with the complex analytic signal has minimal ringing artifacts, as seen in Fig. 5(b). The artifacts are an effect of low-pass filtering in the transverse direction. The high-frequency data is lost when calculating the magnitude of the complex data, thus producing sidelobes of the individual scatterers in the spatial domain. The resulting sidelobes appear as ringing artifacts around each point scatterer.

The minimum norm solution with Tikhonov regularization was acquired using both the magnitude and complex analytic fringe data. The L-curve, the plot of the seminorm $||Lx||_2$ versus the residual norm $||Ax-b||_2$, is a means of displaying the influence of a regularization and aids in choosing an appropriate regularization parameter, λ [34]. Several values for the regularization parameter were explored, but $\lambda = 0.02$ optimally balanced the seminorm with the residual norm when $L = I$. Fig. 6(a) shows the reconstruction based on only the magnitude data. Reconstruction artifacts such as ringing are somewhat apparent in this image, whereas the reconstruction with the complex analytic signal has minimal ringing artifacts, as seen in Fig. 6(b).

The Richardson–Lucy algorithm was implemented, and comparisons demonstrate the improvement of blurry regions of the image with increasing number of iterations. The Richardson–Lucy algorithm makes use of only the magnitude fringe data since it has a positivity constraint for each iteration. Fig. 7(a) shows the magnitude data reconstruction for one iteration of the Richardson–Lucy algorithm. Comparatively, since Gaussian beam blurring is a physical parameter, a number of iterations can be associated with each focal depth in the lens. Fig. 7(b) shows the magnitude for a dynamically iterative reconstruction where the number of iterations is depth dependent. Specifically, the iterations increase proportional to the size of the Gaussian blurring kernel from 1 to 21. This method was chosen by monitoring the convergence of the absolute difference images at each iteration $||y_{i+1} - y_i||_2$. Other authors have addressed the optimality criterion for

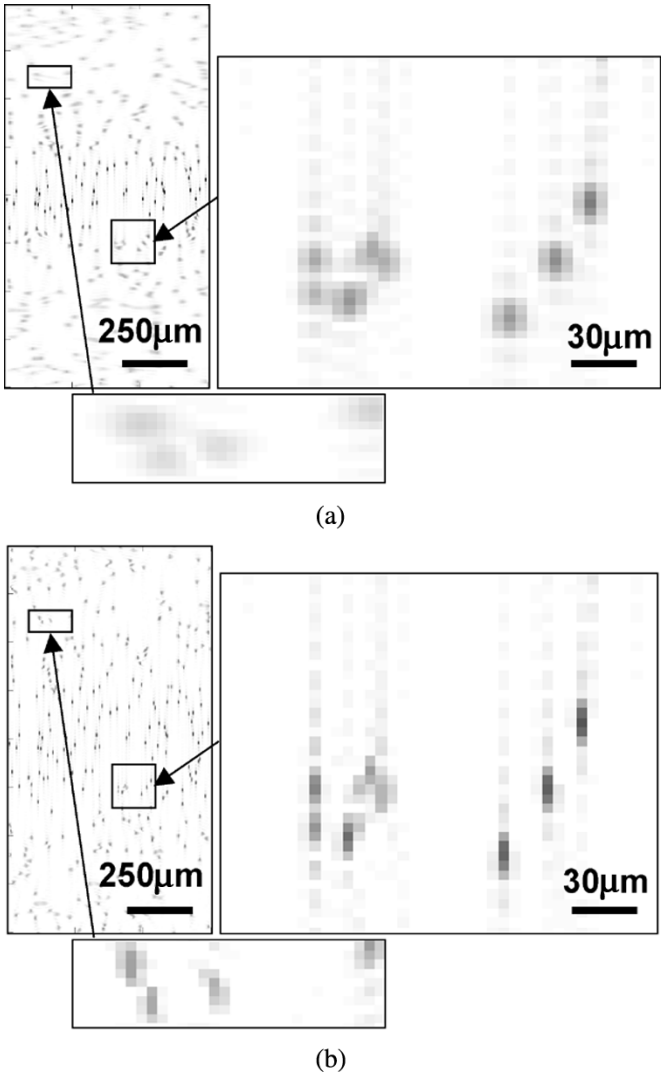

Fig. 7. Richardson–Lucy reconstruction using magnitude data, SNR $= 35$ dB, for (a) one iteration and for (b) depth-dynamic iterations (1 to 21 linearly spaced from focus to image edge).

TABLE I
MEAN-SQUARE ERROR OF RECONSTRUCTION USING EACH DECONVOLUTION METHOD

Deconvolution Method	Mean Square Error
TSVD magnitude	7.8677e-4
TSVD complex	5.7126e-4
Tikhonov magnitude	6.5790e-4
Tikhonov complex	5.8057e-4
Richardson-Lucy single iteration	8.1952e-4
Richardson-Lucy dynamic iteration	4.7660e-4

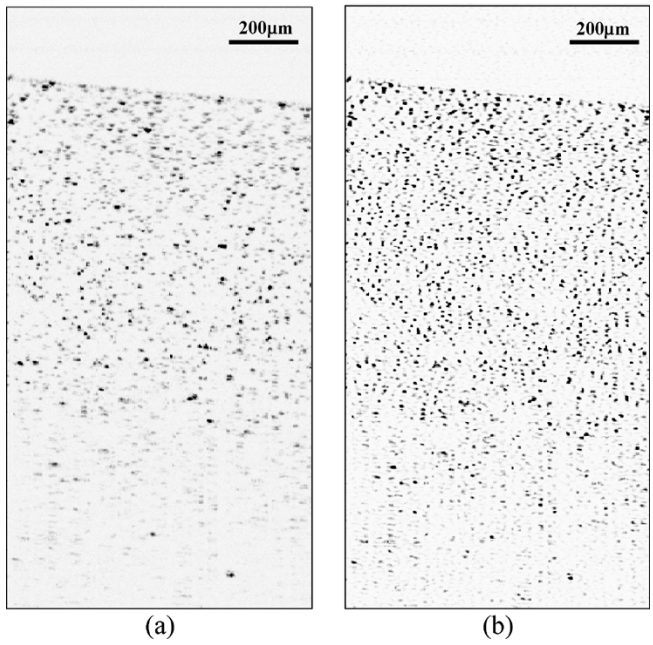

Fig. 8. Application of the dynamic Richardson–Lucy algorithm on a tissue phantom. (a) Original and (b) Richardson–Lucy corrected image.

selecting parameters for algorithms like the Richardson–Lucy, which lead to image convergence [35]. Since Richardson–Lucy sharpens more for each iteration, the parameters are chosen according to a minimum acceptable PSF width, specified by the resolution.

For each of these algorithms, Table I lists and compares the mean-square error

$$E[e^2] = \frac{1}{MN}\sum_{i=1}^{M}\sum_{j=1}^{N}(y(i,j) - x(i,j))^2 \qquad (27)$$

where M and N are the image dimensions. The dynamic Richardson–Lucy algorithm reconstructs the image with the minimum mean-square error of all the tested algorithms. These results provide quantitative justification for employing the dynamically iterative algorithm on real data.

V. EXPERIMENTAL DATA

A tissue phantom was designed to test the PSF of our experimental setup. To design an appropriate tissue phantom, it is desirable to include individual scatterers on the size order of cellular structures and near our resolution limit. A solution of 4.0 g of polydimethylsiloxane (PDMS) was mixed with 7 mg of Magnetite (Fe_3O_4), each having an average diameter of 1.9 μm. These microparticles act as point scatterers in OCT, thus providing a physical embodiment of our simulated experiment. Furthermore, these microparticles are used to simulate individual cells/nuclei in engineered tissues [8]. Images were taken at an axial scan rate of 25 Hz, with a lens having a 20-mm focal length and a 6-mm diameter, a system bandwidth of 100-nm FWHM, a center wavelength of 800 nm, and 15.6 mW of power incident on the sample. The width of the unfocused beam incident on the lens is 1.3 mm, which dictates a NA of 0.065 in free space. The calculated axial resolution is 3 μm, the transverse resolution was 15 μm, and the confocal region was 430 μm. Since the Richardson–Lucy algorithm provides the best results in the simulations, Fig. 8 shows the original and Richardson–Lucy corrected images. The final deblurred region can be estimated by measuring the distance of the resolved points outside of the confocal region. The criteria for determining a resolved

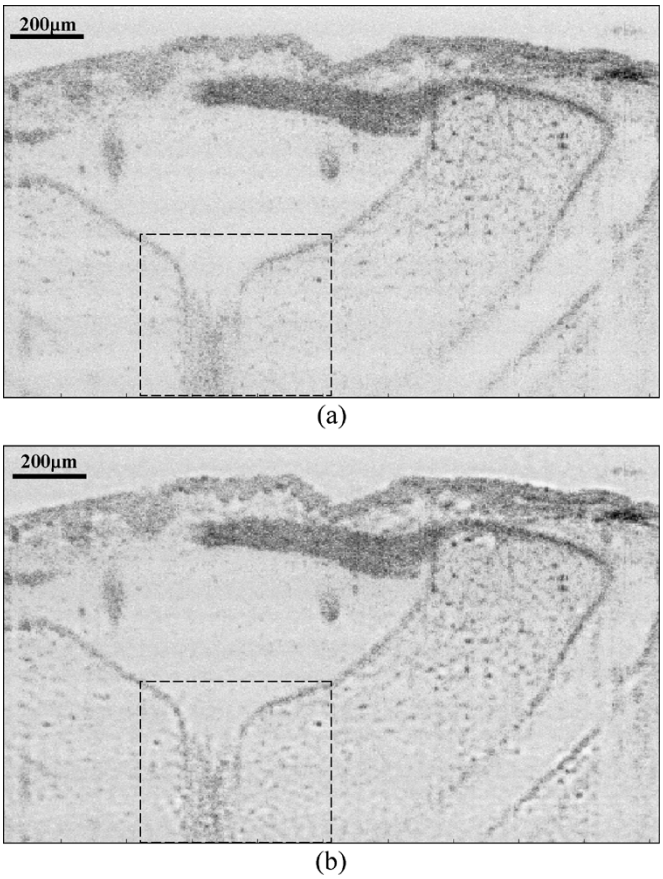

Fig. 9. Application of the dynamic Richardson–Lucy algorithm to *in vivo* cellular data. OCT images of the mesenchymal cells of the *Xenopus laevis*, represented (a) without deconvolution and (b) with the dynamic Richardson–Lucy algorithm. Comparison of cellular feature within the dashed box outside the confocal region shows more distinct cell boundaries and features in (b).

point is that the energy compaction of particles outside of the confocal region in the new image is equivalent to the energy compaction of particles on the edge of the confocal region in the original image. Based on this image data, the deblurred region extended over 500 μm above and below the confocal region, or a total distance of approximately 1.43 mm.

A second experiment was conducted by acquiring OCT image data from an *in vivo Xenopus laevis* (African frog) tadpole, a common developmental biology animal model and one used routinely for demonstrating OCT imaging performance [6]. Imaging along the dorsal surface of the tadpole, details of mesenchymal cells were imaged with a 20-mm focal length lens at an axial scan rate of 40 Hz. The image has the same corresponding axial and transverse resolutions, and, therefore,the same confocal parameter, as the previous image (Fig. 8). Fig. 9 illustrates the original and corrected images.

The original image exhibits a widening transverse PSF out of the confocal region due to the effect of the Gaussian beam, which spreads the energy of a cellular boundary or feature across several pixels, thus blurring and misrepresenting the cellular structure. By comparing cellular regions outside of the confocal region in the two images [boxed regions in Fig. 9(a) and (b)], the boundaries of the cell membranes and the nuclei appear more distinct in the deconvolved image [Fig. 9(b)].

VI. Conclusion

In this paper, we have demonstrated several deconvolution methods for mitigating the transverse blurring in OCT. From the simulations, both the regularized solutions and the Richardson–Lucy algorithm solution produce comparable results, although there is a drawback to the regularized solution when using the acquired data, which seems to be a result of phase instability among acquired adjacent axial scans. The Richardson–Lucy algorithm appears to be more robust to these errors since the unstable phase fronts among axial scans do not greatly modify the magnitude image. Ideally, phase stable measurements are important for continued work with the regularized solution. Furthermore, a complete solution to the inverse scattering problem is likely the next step for improving performance of the regularized solution. This is because a complete regularized solution would assume a strict model, whereas the dynamic Richardson–Lucy algorithm assumes an approximated model.

Some of the limitations of the Richardson–Lucy algorithm are a result of our inability to incorporate speckle noise, dispersion, multiply-scattered light, and limited bandwidths into the algorithm. Yet, it offers the lowest mean-squared-error compared to the other deconvolution methods evaluated. This is because the algorithm tends to concentrate energies near boundaries, which provides a good approximation to cellular boundaries and subcellular features, and tends to be more robust against errors from the defocused blur. The Richardson–Lucy algorithm deblurs the intensity of an image, therefore concentrating the power near the strong scatterers. These strong scatterers often correspond to the cell nuclei and membranes. Therefore, the implementation of a dynamically iterative Richardson–Lucy algorithm performs well for distinguishing physical features of the specimen at the cellular level. In particular, the transverse deblurring effect of this algorithm can extend the apparent confocal region of the image, providing less transverse blurring in the OCT image over extended distances, without the need for implementing new optical hardware or the acquisition, segmentation, and assembly of multiple OCT images from the same specimen. The improvements afforded by a dynamically applied Richardson–Lucy algorithm are most pronounced when imaging specimens at the cellular level and at the resolution limits afforded by current OCT systems.

Acknowledgment

The authors would like to thank A. Oldenburg, R. Stack, and W. Luo from the Beckman Institute for Advanced Science and Technology for their technical contributions to this research, as well as C. Xu for his careful review of this manuscript.

References

[1] V. Kumar, N. Fausto, and A. Abul, *Robbins & Cotran Pathologic Basis of Disease*, 7th ed. Philadelphia, PA: Saunders, 2004.

[2] J. P. Vacanti and R. Langer, "Tissue engineering: the design and fabrication of living replacement devices for surgical reconstruction and transplantation," *Lancet*, vol. 354, pp. SI32–SI34, 1999.
[3] D. Huang, E. A. Swanson, C. P. Lin, J. S. Schuman, W. G. Stinson, W. Chang, M. R. Hee, T. Flotte, K. Gregory, C. A. Puliafito, and J. G. Fujimoto, "Optical coherence tomography," *Science*, vol. 254, pp. 1178–1181, 1991.
[4] J. M. Schmitt, "Optical coherence tomography (OCT): a review," *IEEE J. Sel. Topics Quantum Electron.*, vol. 5, no. 4, pp. 1205–1215, Jul./Aug. 1999.
[5] B. E. Bouma and J. G. Tearney, *The Handbook of Optical Coherence Tomography*. New York: Marcel-Dekker, 2001.
[6] S. A. Boppart, B. E. Bouma, C. Pitris, G. J. Tearney, J. F. Southern, M. E. Brezinski, and J. G. Fujimoto, "*In vivo* cellular optical coherence tomography imaging," *Nature Med.*, vol. 4, pp. 861–864, 1998.
[7] S. A. Boppart, M. E. Brezinski, C. Pitris, and J. G. Fujimoto, "Optical coherence tomography for neurosurgical imaging of human intracortical melanoma," *Neurosurgery*, vol. 43, pp. 834–841, 1998.
[8] W. Tan, A. Sendemir-Urkmez, L. J. Fahrner, R. Jamison, D. Leckband, and S. A. Boppart, "Structural and functional optical imaging of three-dimensional engineered tissue development," *Tissue Eng.*, vol. 10, pp. 1747–1756, 2004.
[9] Z. Chen, Y. Zhao, S. M. Srinivas, J. S. Nelson, N. Prakash, and R. D. Frostig, "Optical Doppler tomography," *IEEE J. Sel. Topics Quantum Electron.*, vol. 5, no. 4, pp. 1134–1141, Jul./Aug. 1999.
[10] A. V. Zvyagin, J. B. Fitzgerald, K. K. M. B. D. Silva, and D. D. Sampson, "Real-time detection for Doppler optical coherence tomography," *Opt. Lett.*, vol. 25, pp. 1645–1647, 2000.
[11] Y. Zhao, Z. Chen, C. Saxer, S. Xiang, J. F. de Boer, and J. S. Nelson, "Phase-resolved optical coherence tomography and optical Doppler tomography for imaging blood flow in human skin with fast scanning speed and high velocity sensitivity," *Opt. Lett.*, vol. 25, pp. 114–116, 2000.
[12] L. B. Lucy, "An iterative technique for rectification of observed distributions," *Astron. J.*, vol. 79, pp. 745–765, 1974.
[13] W. H. Richardson, "Bayesian-based iterative method of image restoration," *J. Opt. Soc. Amer.*, vol. 62, pp. 55–59, 1972.
[14] J. A. Izatt, M. R. Hee, G. M. Owen, E. A. Swanson, and J. G. Fujimoto, "Optical coherence microscopy in scattering media," *Opt. Lett.*, vol. 19, pp. 590–592, 1994.
[15] J. L. Starck and E. Pantin, "Deconvolution in astronomy: a review," *Pub. Astron. Soc. Pacific*, pp. 1051–1069, 2002.
[16] P. Shaw, "Deconvolution in 3-D optical microscopy," *Histochem. J.*, vol. 26, pp. 687–694, 1994.
[17] M. D. Kulkarni, C. W. Thomas, and J. A. Izatt, "Image enhancement in optical coherence tomography using deconvolution," *Electron. Lett.*, vol. 33, pp. 1365–1367, 1997.
[18] D. L. Marks, A. L. Oldenburg, J. J. Reynolds, and S. A. Boppart, "Digital algorithm for dispersion correction in optical coherence tomography for homogeneous and stratified media," *Appl. Opt.*, vol. 42, pp. 204–217, 2003.
[19] T. Blu, H. Bay, and M. Unser, "A new high-resolution processing method for the deconvolution of optical coherence tomography signals," presented at the IEEE Int. Symp. Biomedical Imaging, Washington, DC, 2002.
[20] B. Hermann, E. J. Fernandez, A. Unterhuber, H. Sattmann, A. F. Fercher, W. Drexler, P. M. Prieto, and P. Artal, "Adaptive-optics ultrahigh-resolution optical coherence tomography," *Opt. Lett.*, vol. 29, pp. 2142–2144, 2004.
[21] Z. Ding, H. Ren, Y. Zhao, J. S. Nelson, and Z. Chen, "High-resolution optical coherence tomography over a large depth range with an axicon lens," *Opt. Lett.*, vol. 27, pp. 243–245, 2002.
[22] Y. Wang, Y. Zhao, J. S. Nelson, and Z. Chen, "Ultrahigh-resolution optical coherence tomography by broadband continuum generation from a photonic crystal fiber," *Opt. Lett.*, vol. 28, pp. 182–184, 2003.
[23] W. Drexler, U. Morgner, F. X. Kartner, C. Pitris, S. A. Boppart, X. D. Li, E. P. Ippen, and J. G. Fujimoto, "*In vivo* ultrahigh-resolution optical coherence tomography," *Opt. Lett.*, vol. 24, pp. 1221–1223, 1999.
[24] M. E. Brezinski, G. J. Tearney, S. A. Boppart, E. A. Swanson, J. F. Southern, and J. G. Fujimoto, "Optical biopsy with optical coherence tomography: feasibility for surgical diagnostics," *J. Surg. Res.*, vol. 71, pp. 32–40, 1997.
[25] S. A. Boppart, W. Luo, D. L. Marks, and K. W. Singletary, "Optical coherence tomography: feasibility for basic research and image-guided surgery of breast cancer," *Breast Cancer Res. Treat.*, vol. 84, pp. 85–97, 2004.
[26] L. K. Jensen, L. Thrane, P. E. Andersen, A. Tycho, F. Pedersen, S. Andersson-Engels, N. Bendsoe, S. Svanberg, and K. Svanberg, "Optical coherence tomography in clinical examinations of nonpigmented skin malignancies," in *Proc. SPIE Optical Coherence Tomography and Coherence Techniques*, vol. 5140, 2003, pp. 160–167.
[27] B. E. A. Saleh and M. C. Teich, *Fundamentals of Photonics*. New York: Wiley, 1991.
[28] R. E. Blahut, *Theory of Remote Image Formation*. Cambridge, U.K.: Cambridge Univ. Press, 2004.
[29] Y. Bresler, S. Basu, and C. Couvreur, *Hilbert Spaces and Least Squares Methods for Signal Processing*, to be published.
[30] D. P. O'Leary, "Near-optimal parameters for Tikhonov and other regularization methods," *SIAM J. Sci. Comput.*, vol. 23, pp. 1161–1171, 2001.
[31] C. R. Vogel, *Computational Methods for Inverse Problems*. New York: SIAM, 2002.
[32] L. A. Shepp and Y. Vardi, "Maximum likelihood reconstruction for emission tomography," *IEEE Trans. Med. Imag.*, vol. MI-1, no. 2, pp. 113–122, Oct. 1982.
[33] D. L. Snyder, T. J. Schultz, and J. A. O'Sullivan, "Deblurring subject to nonnegativity constraints," *IEEE Trans. Signal Process.*, vol. 40, no. 5, pp. 1143–1150, May 1992.
[34] P. C. Hansen, "Numerical tools for analysis and solution of Fredholm integral equations of the first kind," *Inv. Probl.*, vol. 8, pp. 849–872, 1992.
[35] I. Csiszar, "Why least squares and maximum entropy?," *Ann. Stat.*, vol. 19, pp. 2032–2066, 1991.

Tyler S. Ralston (A'98) was born in Dayton, OH, in 1977. He received the B.S. degree in electrical and computer engineering from the University of Dayton, Dayton, in 2000, and the M.S. degree in electrical and computer engineering from the University of Illinois at Urbana-Champaign (UIUC) in 2004. He is currently pursuing the Ph.D. degree at UIUC.

Prior to his masters studies, he was with the medical products sector at Battelle Memorial Institute, Columbus, OH. He holds a fellowship at the Beckman Institute for Advanced Science and Technology, UIUC. His research interests include both signal processing and inverse problems for optical biomedical imaging.

Mr. Ralston has previously served on the board for the student chapter of IEEE and is currently president of the student chapter of the OSA at UIUC. He earned a "Key Contributor" award for production of a medical instrument while with the medical products sector at Battelle Memorial Institute.

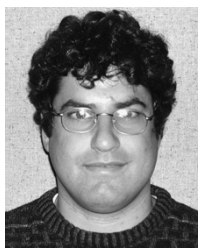

Daniel L. Marks was born in Chicago, IL, in 1973. He received the B.S., M.S., and Ph.D. degrees in electrical engineering from the University of Illinois at Urbana-Champaign (UIUC) in 1995, 1998, and 2001, respectively.

He is currently a Visiting Research Scientist with the Biophotonics Group, Beckman Institute, UIUC. His main research interest is the design and implementation of optical sensing systems, encompassing both the physical apparatus and the mathematics of inference methods. This work includes optical coherence tomography, 3-D optical tomography, and nonlinear spectroscopy.

Dr. Marks was awarded a National Science Foundation Graduate Fellowship.

Farzad Kamalabadi (M'02) received the B.S. degree in computer systems engineering from the University of Massachusetts, Amherst, in 1991, and the M.S. and Ph.D. degrees in electrical engineering from Boston University, Boston, MA, in 1994 and 2000, respectively.

Since 2000, he has been an Assistant Professor with the Department of Electrical and Computer Engineering, University of Illinois, Urbana-Champaign. He was a Visiting Fellow with SRI International in Fall 2002 and a National Aeronautics and Space Administration (NASA) Faculty Fellow with the Jet Propulsion Laboratory, California Institute of Technology, Pasadena, in Summer 2003. He has served in various organizational capacities, including Session Organizer and Chair for the International Union of Radio Science special sessions on Ionospheric Imaging in 2003 and 2004. His research interests include multidimensional and statistical signal processing; inverse problems in image formation, sensor array processing, and tomography; and the development of optical and radio sensing and imaging techniques and their applications to space physics, astronomy, and medicine.

Dr. Kamalabadi received a National Science Foundation (NSF) Fellowship in 1994, a Best Student Paper Award in 1997, a NASA fellowship in 1998, and an NSF Faculty Early Career Development (CAREER) Award in 2002.

Stephen A. Boppart (M'90) was born in Harvard, IL, in 1968. He received the B.S. degree in electrical engineering with a minor in bioengineering and the M.S. degree in electrical engineering from the University of Illinois at Urbana-Champaign (UIUC) in 1990 and 1991, respectively, the Ph.D. degree in medical and electrical engineering from the Massachusetts Institute of Technology, Cambridge, in 1998, and the M.D. degree from Harvard Medical School, Cambridge, in 2000.

Prior to his doctoral studies, he conducted research on laser-tissue interactions at the Air Force Laser Laboratory, Brooks Air Force Base, TX. Currently, he is an Assistant Professor of electrical engineering and a Research Physician of Internal Medicine at UIUC. He also holds appointments at the Beckman Institute for Advanced Science and Technology, in the Department of Bioengineering, the Center for Nanoscale Science and Technology, the Institute of Genomic Biology, the Neuroscience Program, and the College of Medicine at the University of Illinois. He has authored over 90 papers and book chapters, over 225 invited and contributed presentations, and holds over ten patents in the area of optical biomedical imaging. His current research interests include novel optical molecular imaging technologies and their applications in cancer detection and tissue engineering.

Prof. Boppart is a member of the IEEE Engineering in Medicine and Biology Society, OSA, SPIE, AAAS, the Society for Molecular Imaging, the American Association for Cancer Research, the American College of Physicians, and the American Medical Association. In 2002, he was recognized as one of the Top 100 Innovators in the World by MIT's *Technology Review* magazine.